JOURNAL OF GEOPHYSICAL RESEARCH, VOL. ???, XXXX, DOI:10.1002/,

Equatorial *F*-region plasma waves and instabilities observed near midnight at solar minimum during the NASA Too WINDY sounding rocket experiment

D. L. Hysell[1], S. Rao[1], and M. F. Larsen[2]

[1]Earth and Atmospheric Sciences, Cornell University, Ithaca, NY, USA

[2]Physics and Astronomy, Clemson University, Clemson, SC, USA

Abstract. Radar and sounding rocket observations of plasma irregularities in the *F*-region ionosphere acquired on June 19, 2019, during NASA experiment Too WINDY on Kwajalein Atoll are presented. The experiment was conducted near local midnight during a period of low solar flux and quiet geomagnetic conditions. Plasma density irregularities were seen by the rocket and also in the incoherent scatter radar data to emerge and persist mainly in the topside. Density irregularities in the bottomside remained very small by comparison throughout the observations. Zonal plasma drifts measured by the rocket were highly structured in the topside. Patches of coherent scatter entrained in the large-scale topside density irregularities appeared to propagate slowly westward in a narrow flow channel detected by the rocket. Broadband ELF emissions were also detected in the topside. Some of the characteristics of the topside irregularities are typical of postsunset equatorial *F* region irregularities observed frequently by coherent scatter radars, and some of the common features in the coherent scatter database are reviewed. Two scenarios that have been proposed to account for postmidnight spread *F* are tested computationally. One involves unseasonably large background zonal electric fields, and the other involves forcing from below by neutral waves and turbulence. Neither scenario appears to be able to account for the Too WINDY observations and the preponderance of topside irregularities without bottomside precursors in particular.

Introduction

The NASA Too WINDY sounding rocket experiment was conducted from Kwajalein Atoll between June 9–19, 2019. The experiment was the successor to WINDY (Waves and Instabilities from a Neutral Dynamo) which was conducted two years earlier [*Hysell et al.*, 2020]. The purpose of both experiments was to study the postsunset conditions surrounding the onset of convective instability in the *F* region ionosphere (e.g., *Woodman* [2009]; *Kelley et al.* [2011] and references therein). Such instability is associated with equatorial spread *F* (ESF) and related phenomena which can degrade the performance of a number of vital radio communication, navigation, and imaging systems. The ability to forecast ESF is a critical but elusive space-weather milestone (e.g., *Retterer* [2005]; *Makela et al.* [2006]).

The focus of WINDY and Too WINDY was on the role of vertical current in the *F* region driven by an imperfectly efficient *F* region dynamo and the attendant vertical shear in the zonal flow [*Kudeki et al.*, 1981; *Tsunoda et al.*, 1981; *Haerendel et al.*, 1992; *Haerendel and Eccles*, 1992]. Analysis and numerical simulation show that irregularity formation is substantially accelerated when the current and the shear flow are present [*Hysell and Kudeki*, 2004; *Kudeki et al.*, 2007; *Aveiro et al.*, 2012]. Instability is most robust in the vicinity of sheared flow but can excite the conventional convective instability in a bootstrapping process, leading to the production of topside depletion plumes. The mechanism can also account for so-called “bottom-type” layers in the valley region known to be precursors of depletion plumes and other ESF telltales [*Woodman and La Hoz*, 1976]. Radar data acquired throughout the WINDY experiment were consistent with this scenario and provided new information about the large-scale clustering of depletion plumes often observed.

The vehicle carrying the WINDY instrumented payload failed, and so Too WINDY was conducted two years later in June solstice when the range became available. This season is not prone to ESF activity on Kwajalein. More importantly, the 10.7 cm solar flux index had decreased to just 68-72 by the time of the experiment. The occurrence rate of post-sunset irregularities was much lower than it had been during WINDY, and plasma number densities were also much lower. Irregularity occurrence also shifted later in the postsunset sector toward midnight. This changed the focus of the Too WINDY experiment.

We report here on the results of the experiment which was conducted just prior to midnight **on June 19, 2019**. A chemical release rocket was launched to deploy lithium and trimethyl aluminum (TMA) trails for measuring neutral winds in the thermosphere and mesosphere/lower thermosphere (MLT), respectively. Following that, an instrumented rocket carrying a Langmuir probe, a magnetometer, and an electric field instrument was launched. The condition for launch was the observations of coherent scatter from field-aligned irregularities in the *F* region by the ALTAIR high-power, large-aperture (HPLA) radar which also provided incoherent-scatter measurements of the ionosphere in a west-to-east scan format. A Fabry Perot interferometer and a Digisonde were also run during the experiment.

Remarkably, irregularities were observed by the rockets and the radar mainly in the topside ionosphere with only a little evidence of instability or structuring in the bottomside. This defies expectations for plasma convective instability but could be consistent with a number of observations of postmidnight irregularities from the Jicamarca Radio Observatory which has amassed a large database of solar-minimum observations. Below, we examine data from ALTAIR and from the instrumented rocket and develop a scenario that could explain them and inform the long-term datasets acquired at Jicamarca and elsewhere.

ALTAIR radar observations

The Too WINDY experiment was supported by the ARPA Long-Range Tracking and Instrumentation (ALTAIR) Radar *(8.72°N, 167.73° E)* which provided invaluable context. This is a fully-steerable, dual frequency (158 and 422 MHz), high-power, large-aperture radar capable of observing incoherent scatter as well as coherent scatter from field-aligned plasma density irregularities when its beam is pointed perpendicular to the magnetic field. The ALTAIR operating modes available for ionospheric research were reviewed recently by *Hysell et al.* [2020]. Most of the data acquired on the rocket launch night were acquired in the VEP 3-300 (VHF) and UEP 3-300 (UHF) modes. These employed 300 μs pulses with 3-bit Barker coding and a 67 Hz pulse repetition frequency and are processed with an effective 15-km range resolution. Scans were made in the plane perpendicular to the magnetic field. Individual scans took just under 10 min. to complete. One observable is electron density which is estimated from range-corrected power measurements involving an established calibration constant. The calibration was tested through comparison with a nearby sounder **(Digisonde DPS-4)**. The other observable is the intensity of coherent scatter from field-aligned plasma density irregularities in the field of view.

Hysell et al. [2020] describe an almost unbroken sequence of nights of vigorous convective instability as seen by the ALTAIR radar in **August and September** of 2017 during the WINDY project. At that time, the 10.7 cm solar flux index varied between 90–130. Electron densities were also highly variable during WINDY, and coherent scatter and depletion plumes were nearly ubiquitous from night to night. A regular sequence of events played out each night as bottom-type layers evolved into bottomside irregularities and then topside depletions and plumes.

The scenario was very different in the **summer** of 2019 during project Too WINDY. The 10.7 cm solar flux index varied between 68–72, and conditions were geomagnetically quiet.

The postsunset *F* region ionosphere was much lower and more rarefied than it had been two years prior, and instances of convective instability and spread *F* conditions were rare. Vigorous instability like the cases described by *Hysell et al.* [2020] occurred only once during the Too WINDY campaign, but clear optical conditions required by the experiment were not present at the time. Suitable optical conditions emerged only on the last night of the experimental window, June 19, 2019, and then only late in the evening when number densities (and corresponding radar signal to noise ratios) were very low.

Fig. 1 shows a series of UHF radar scans beginning around the time of the rocket launches. Each scan is a representation of electron number density. Plotted lines to the right of the scans show number density profiles through the center of the corresponding scans. Bright patches indicate coherent scatter which was only prominent in the last of the scans where it can be seen in the topside. Some structuring is evident in the *F*-region bottomside, particularly on the western side, in most of the scans. More dramatic structuring exists in the topside. The last scan shows intense topside structuring reminiscent of depletion plumes characteristic of spread *F* conditions. The topside coherent scatter in the final scan of the evening lies at the edge of a topside density depletion.

Fig. 2 shows VHF observations for the same scans depicted in Fig. 1. Sky noise is much stronger at VHF than at UHF, and the electron density estimates derived from VHF data have larger uncertainty than those derived from UHF. However, coherent scatter tends to be much stronger at VHF than at UHF due to the stronger diffusive dissipation associated with the UHF wavelength. Fig. 2 shows patchy coherent scatter, mainly in the topside, throughout the sequence of scans. The emergence of coherent scatter, together with the onset of bottomside density structuring, triggered the launch of the Too WINDY rockets.

The last four VHF scans depict the emergence and subsequent motion of a coherent scatter patch in the topside to the east of ALTAIR. The patch can be seen to be drifting slowly westward by the end of the experiment. We note that westward-drifting plumes are common in the postmidnight sector during low solar-flux conditions in the Jicamarca database. An example of this will be presented later in the paper.

For the sake of completeness, Fig. 3 shows an oblique UHF radar scan depicting a small cluster of depletion plumes observed on June 12, 2019. This event developed following the same sequence of events observed throughout the 2017 WINDY campaign [*Hysell et al.*, 2020], exhibiting further growth and development in scans taken after the one shown. It is remarkable only in that is was the lone example of robust postsunset ESF observed during Too WINDY.

Instrumented rocket data

The Too WINDY mission involved the launch of a chemical-release rocket and an instrumented rocket in rapid succession. Both vehicles were Black Brant Xs. The chemical-release rocket deployed TMA and lithium for measuring neutral winds in the mesosphere-lower-thermosphere (MLT) and thermosphere regions, respectively. Both rockets were launched to the northwest. Results from the chemical releases will be presented in a separate manuscript.

The instrumented rocket included a fixed-bias Langmuir probe, a fluxgate magnetometer, and an electric field instrument comprised of two orthogonal stacer boom pairs with 6 tip-to-tip separations. The vehicle had a magnetic attitude control system and flew in cartwheel mode, its body aligned parallel to the geomagnetic field and its electric field booms in the plane perpendicular to the magnetic field. The spin rate after despin and boom deployment was approximately 0.6 rotations per second. Apogee for the instrumented rocket, which was launched at 11:26:46 UT, was approximately 410 km.

The Langmuir probe was a 1 3/4” sphere deployed on the end of an axially mounted, forward looking 1” diameter fiberglass boom. The signal derived from the probe current passed through four independent amplifiers with different gain settings which were sampled at 5,000 samples per second. Nosecone deployment completed at about 125 km altitude at which time data became available. Electron density data were calibrated using measurements from ALTAIR.

Electron density estimates derived from the Langmuir probe are shown in Fig. 4 which presents the base-10 logarithm of electron density versus altitude. The curves show that the electron density peak was at about 250 km altitude with a decreasing trend in peak number density to the west. The most discernible irregularities were in the topside, mainly between 300-325 km and above 350 km altitude in the upleg and downleg. Subtle bottomside irregularities are also evident in the upleg around 175 km and downleg around 200 km. A sporadic E layer was detected on the downleg around 110 km altitude.

Electric field information was derived from spherical probes on the crossed stacer booms which were connected to differential amplifiers and filtered and sampled at several different rates. The data were despun with the aid of measurements form a horizon-crossing indicator (HCI) upon which the attitude solution was based. The electric fields were shifted from the rocket to the earth-fixed frame of reference using trajectory information from a GPS receiver along with magnetic field measurements from the fluxgate magnetometer.

Fig. 5 shows vector electric field estimates for the upleg and downleg which were filtered and sampled at a rate of 1250 samples per second. Boom deployment was not complete and settled until the rocket passed through about 250 km altitude. Thereafter, the instrument indicates that the ionosphere was descending throughout the upleg at a rate as fast as 100 m/s near apogee. The descent was quite variable and much slower during most of the downleg. Irregularities can be found in the vertical and zonal drifts mainly between 300-325 km and above 350-km altitude with some modest irregularities present near 200 km altitude on the downleg.

The zonal drift was as fast as about 150 m/s eastward near and above the *F* peak, decreasing to about 60 m/s eastward in the valley region. Although the vertical shear in the zonal drifts in the bottomside was significant, the flow did not reverse to westward below the *F* peak as it often does in the postsunset sector. The most distinct dynamical feature in the zonal drifts is a stratum of slowly-drifting plasma above 350 km altitude where the flow shifted from eastward to westward. This was observed on the upleg and and at slightly higher altitude on the downleg. The stratum coincides in altitude with the westward-drifting patch of coherent scatter seen by ALTAIR late in the experiment.

Electric field spectra in the ELF band for the flight are shown in Fig. 6. These spectra represent periodograms computed from data from a single electric field boom which were low-pass filtered in hardware prior to sampling at 5,000 samples per second. The most noteworthy features in the band are signatures of ELF hiss. The strongest hiss was observed between 200–450s flight time when the vehicle was above 350 km altitude. As the figure indicates, the hiss fell mainly between the first gyroharmonic frequencies for helium and hydrogen ions. There is a distinct absence of spectral features at the second helium gyroharmonic frequency. Another dead band arguably exists at the first hydrogen gyroharmonic frequency although there is little spectral energy density at frequencies higher than Ω_{H^+} for contrast.

ELF spectrograms were also computed for data from the Langmuir probe and the fluxgate magnetometer. Aside from some obvious instrumental interference, there were no significant spectral features in the ELF data from either instrument. The absence of features in the ELF density data is consistent with the electromagnetic nature of the waves in the E-field data. The absence of features in the magnetometer data is consistent with the relative lack of sensitivity of the magnetometer at ELF frequencies. The noise level of the magnetometer was at the level of 1 $(nT)^2$/Hz using even relatively broad time and frequency bin averaging. This is well above the amplitude of the equatorial noise signatures observed by magnetometers on the Van Allen and Demeter satellites (see for example *Pfaff et al.* [2008]; *Miyoshi et al.* [2019]).

Contextual data from Jicamarca and elsewhere

We can place the too WINDY observations in a broader experimental context. The Jicamarca Radio Observatory makes regular nighttime observations of coherent scatter from ionospheric irregularities *(11.95° S, 76.87° W)*. A sizeable database exists for low solar flux conditions in all seasons. Observations were made throughout the too WINDY campaign, for example. While the Jicamarca data are representative of a different longitude sector, they give an indication of the effect of very low solar flux conditions on typical irregularity phenomenology.

The climatology of plasma density irregularities associated with ESF versus season and solar cycle has been assessed using in situ satellite measurements (e.g., *Gentile et al.* [2006]), ground-based measurements of radio scintillation, and ground-based radar and sounder measurements (e.g., *Chapagain et al.* [2009]), among other approaches. Satellite measurements inform the frequency distribution of just those irregularities that reach the satellite altitude, a factor highly dependent on solar flux. Both scintillation and sounder measurements are most sensitive to plasma irregularities where background number densities are high and so imply another bias. HPLA radars can detect field-aligned irregularities at all altitudes and in very rarefied plasmas and so give relatively unbiased climatology information. The impact of solar flux on ESF climatology assessed using HPLA radars is much less drastic than that indicated by other experimental methodologies. Only HPLA radars observe bottom-type scattering layers. However, the sensitivity of HLPA radars to field-aligned irregularities increases with wavelength, all other parameters being equal. We expect Jicamarca to be a more sensitive indicator of plasma density irregularities than ALTAIR VHF or UHF.

During June solstice under low solar-flux conditions, irregularity occurrence in the Peruvian sector is reduced and shifts dramatically from the premidnight to the postmidnight sector [*Zhan et al.*, 2018]. During the Too WINDY campaign, Jicamarca observed radar plumes associated with ESF on several evenings after midnight but only twice before midnight. Bottom-type layers, which generally serve as precursors of radar plumes, were largely absent in the observations. In these ways, the Jicamarca and ALTAIR ionospheric observations were comparable during Too WINDY. Most remarkably, post-midnight irregularities generally occurred near the F peak or in the topside without obvious connection to or precursors in the bottomside.

A representative observation of postmidnight field-aligned plasma density irregularities from the morning of June 21, 2019 is shown in Fig. 7 in range-time-intensity (RTI) format. The coherent backscatter in this event arrived mainly from altitudes between 250–450 km altitude. The Doppler shifts of the echoes were indicative mainly of slow ascent with a slow, periodic variation in time. The echo morphology seems more layer-like than plume-like even though the altitudes of the echoes are mainly in the topside. Similar findings have been reported based on observations from the Gadanki radar in India [*Patra et al.*, 2009], the Kototabang radar in Indonesia [*Otsuka et al.*, 2009], and the Sanya radar in Hainan, China [*Li et al.*, 2012]. A summary of radar observations of postmidnight irregularities was presented recently by *Otsuka* [2018].

In fact, the RTI format used in Fig. 7 and the aforementioned references can be deceptive, as the coherent scatter over Jicamarca actually came from a few discrete patches rather than from layers. This can be seen in the radar imagery shown in in Fig. 8. The images shown here were constructed using aperture synthesis imaging methods (e.g., *Hysell and Chau* [2006]). The patches in the images are generally aligned vertically, sometimes having the form of convective plumes, albeit with interruptions between different vertical strata. Animated sequences of images show that the scattering patches remain near zenith and within the vertical radar beam for long periods of time. This explains the layer-like morphology presented by Fig. 7.

The animated radar imagery further shows substantial variability in the zonal flow in which the patches are embedded. The variability is temporal and spatial, with the flow exhibiting strong vertical shear and multiple shear reversals over time. The zonal flow is mainly westward (eastward) early (late) in the event, although flows in both directions generally coexist. Toward the end of the event, the flow is very slow. The net displacement of the individual patches over time is also small because of the reversals.

The spatial resolution of the pixels in the Jicamarca imagery is of the order of a kilometers in each dimension, and the relatively fine resolution makes it evident that the patches mainly do have the form of small convective plumes. The high resolution and high sensitivity of the observations also reveals the existence of a bottom-type scattering layer during the early part of the event. The bottom-type layer can be seen as a narrow, horizontal string of patches at about 250-km altitude in the first three images in Fig. 8. If they were observed with coarser spatial resolution, the patches in Fig. 8 would resemble the undifferentiated ones in the ALTAIR radar scans. The thin, weak bottom-type layer would likewise be difficult to observe at either ALTAIR radar frequency.

Analysis and interpretation

The main findings of the Too WINDY experiment were as follows. During June solstice when the solar flux index was close to 70, the equatorial ionosphere over Kwajalein Atoll became unstable, producing broadband plasma density irregularities detectable by the ALTAIR radar shortly before midnight. Irregularities were clearly evident in the topside which exhibited significant structuring with a characteristic scale of several hundred kilometers in incoherent scatter scans. Patchy coherent scatter was observed at VHF and less clearly at UHF. The motion of the patches of coherent scatter was unsteady and predominantly westward after midnight. Instruments on a sounding rocket payload detected weak density irregularities in the topside and weaker irregularities in the bottomside. The background vector electric field indicated descent in the *F* layer and sheared zonal flows that were mainly eastward in the *F* region except in a band of topside altitudes where the drift was slow and westward. Sporadic *E* layers were present during the experiment.

Some of the aforementioned findings are similar to observations of postmidnight *F* region plasma irregularities made at Jicamarca during low solar-flux conditions. Most notable features in common are topside echoes without precursor or coincident echoes in the bottomside and highly structured zonal plasma drifts.

The climatological average postsunset background *F*-region vertical plasma drift in **Kwajalein's** sector, season, and solar flux level has no prereversal enhancement and is characterized by descent increasing from about -5 m/s at 8 UT to about -16 m/s by 12 UT [*Scherliess and Fejer*, 1999]. These conditions are not conducive to plasma convective instability, even when the effects of vertical currents are taken into account. A numerical simulation of the ionosphere under the conditions in questions conducted in the manner of *Hysell et al.* [2018] (see below) predicts no irregularity formation by local midnight aside from some minor intermediate-scale structuring at the base of the bottomside. What can account for postmidnight spread *F* under solar-minimum, June-solstice conditions, during Too WINDY or more generally?

The null hypothesis to account for post midnight ESF is that conventional convective instability can occur on nights when the background *F*-region vertical drift is more positive than the **Scherliess and Fejer climatological average, if still modest, and that the late time of occurrence is a consequence of the associated, modest instability growth rate or, equivalently, the long e-folding time. Indeed, C/NOFS vertical plasma drift measurements made during low solar flux conditions indicate a tendency for upward drifts near midnight in some seasons and longitude sectors [*Heelis et al.*, 2010; *Stoneback et al.*, 2011]**.

We have tested the null hypotheses with a numerical simulation. Fig. 9 shows the results of a numerical simulation of the dynamics of the postsunset equatorial ionosphere in the Kwajalein sector conducted under the conditions of Too WINDY. The simulation evolves the number density of four ions (NO^+, O_2^+, O^+, and H^+) together with the electrostatic field in three dimensions. Details about the methods used were given in *Hysell et al.* [2018]. Here, forcing was supplied by winds taken from the Horizontal Wind Model (HWM) [*Drob et al.*, 2015] and background electric fields taken from the Fejer-Scherliess model [*Scherliess and Fejer*, 1999] only with a positive 10 m/s vertical drift offset added. Without the offset, the ionosphere is stable. The 10 m/s figure is arbitrary and is intended for illustrative purposes.

The simulation was initialized at 0800 UT, and the panels in Fig. 9 show conditions at 1130 UT. The features in the simulation, including the background shear flow, the emergence of irregularities first in the valley region and then the bottomside, and the eventual production of narrow, tilted, bifurcated depletion plumes penetrating the topside, are typical of ESF in the postsunset sector. In this case, they were merely slow to develop. The simulation shows that it is possible to produce ESF when climatological conditions are unfavorable so long as the background forcing departs significantly from the climatological average. This may happen frequently in view of the fact that the standard deviation of the equatorial ionospheric vertical drifts is comparable to their mean [*Fejer*, 1997].

However, the dynamics produced here in simulation bear no resemblance to the conditions observed during the Too WINDY experiment. In Too WINDY, irregularities were seen mainly in the topside without obvious bottomside precursors. They were shallow but broad and emerged late with no obvious precursors. While the observations of June 12, 2019 shown in Fig. 3 may be consistent with the null hypothesis, neither the Too WINDY rocket and radar measurements nor the bulk of the Jicamarca postmidnight radar imaging database can be explained this way.

Otsuka [2018] suggests two other possibilities for destabilizing the postsunset equatorial F region when vertical drifts are predicted to be small or downward. One is forcing from below by internal gravity waves. The other is structure in the background meridional winds which may be destabilizing under some circumstances (see *Huba and Krall* [2013] and references therein).

Both of the aforementioned scenarios were investigated with an additional simulation run. This one included strong neutral forcing from atmospheric gravity waves propagating from below into the lower thermosphere. The forcing was extracted from the same two-dimensional simulation of waves and turbulence described in *Hysell et al.* [2018]. In the present simulation, the 2D simulation was extended uniformly into the third dimension, and the original plane of the 2D simulation was tilted with respect to the equatorial plane by 25 degrees. This means that the winds and waves in the neutral simulation have a significant component in the parallel (meridional) direction. The background electric field used for this simulation was the unaltered Fejer-Scherliess field.

The waves were launched as an impulse and only began impinging on the lower thermosphere at about 0930 UT. Fig. 10 shows the state of the ionospheric simulation at 1050 UT at which time the neutral waves and turbulence were beginning to dissipate. Among the effects of the neutral forcing are 1) the creation of sporadic and intermediate layers in the *E* and valley region, 2) the inducement of strong, wavelike plasma flows in the plane perpendicular to the magnetic field, the subsequent inducement of a corrugated bottomside *F* region, and the creation of intermediate-scale irregularities at the base of the *F* region reminiscent of bottom-type layers. It is noteworthy that the response is less severe than in the midlatitude case studied by *Hysell et al.* [2018]. This is due to the relative ineffectiveness of meridional winds to deform the *F* region where the magnetic field lines are nearly horizontal. We note also that the strong neutral forcing was ineffective at generating depletion plumes as in the cases studied by *Hysell et al.* [2014].

The introduction of neutral waves and turbulence in the lower thermosphere and thermosphere together with the presence of irregular meridional winds certainly caused structuring and instability in the postsunset ionosphere in simulation. The irregular zonal flows in simulation exemplified by the middle right panel of Fig. 10 are reminiscent of the profiles in Fig. 5, although the structuring in the former is less abrupt. Moreover, the simulation produced subtle topside density irregularities as seen in the top right panel in Fig. 10. These are a byproduct of the slight rearrangement of the topside by the structured meridional winds which were then further stirred by the concurrent irregular zonal flows. The result is roughly consistent with the density profiles in Fig. 4.

However, the overall congruence between the simulation results in Fig. 10 and the radar observations in Fig. 1 remains poor. The radar data showed no evidence of structuring in the valley region and very little structuring in the bottomside. The simulation, meanwhile, did not reproduce the broad topside structuring clearly evident in the UHF radar data. We have not been able to reproduce a reasonable facsimile of the UHF radar observations from Too WINDY through a combination of background electric field and wind forcing. Just how large-scale structuring can be induced in the topside *F* region, where the background density gradient is shallow, and not in the bottomside, where it is steep, is mysterious and hints at complicated but evidently commonplace dynamics.

An interesting sidelight of the rocket experiment was the observation of broadband ELF emissions in the topside ionosphere. The emissions were seen in the electric field data at frequencies between 100 Hz – 1 kHz. No corresponding features were seen in spectrograms derived from the Langmuir probe data. Features were also not observed in spectrograms derived from magnetometer data, but the fluxgate magnetometer flown for this experiment is not very sensitive at these frequencies and was incorporated in the experiment to make measurements of quasi-DC fields associated with currents flowing around density irregularities.

The broadband emissions are similar to those reported by *Chen et al.* [2020] who presented electric field data in the ELF, VLF, and HF bands acquired by the Communication Navigation Outage Forecast System (C/NOFS) satellite at low geomagnetic latitudes. They attributed the emissions, which were found to be stronger in the nightside than the dayside, to low-frequency whistler-mode hiss (see also [*Chen et al.*, 2017]). They also reported gaps in the spectra near the fundamental and second harmonic cyclotron frequencies of the major ion species, i.e. oxygen, helium, and hydrogen. These were associated with wave damping due to coupling of the whistler modes with ion Bernstein modes (e.g., *Kintner et al.* [1991]). At night, there were sharp cutoffs just above the ion gyrofrequencies. The authors pointed out how the spectra could serve as indicators not only of the presence of different ion species but also of their density and temperature which should influence the width and the depth of the minima, respectively.

Pfaff et al. [2008] also reported on ELF hiss with cutoff frequencies controlled by the local ion composition observed in electric fields measured with the Demeter satellite. In those observations, the hiss vanished in regions where low-frequency electric fields associated with plasma density irregularities characteristic of spread *F* conditions were present. *Miyoshi et al.* [2019] presented observations of equatorial noise emissions in the topside ionosphere made with the Van Allen probes. They associated gaps in the spectra at ion gyroharmonic frequencies with mode conversion to electromagnetic ion cyclotron (EMIC) waves. In particular, they interpreted the gap at twice the helium gyrofrequency to the presence of ions with atomic mass-to-charge ratios of two.

Summary

The NASA Too WINDY sounding rocket experiment took place from Kwajalein Atoll in June, 2019, during low solar flux conditions when the climatological conditions for plasma convective instability leading to equatorial spread *F* were generally unfavorable. Practical considerations, poor meteorological conditions mainly, led to rocket launches taking place late in the campaign window and late at night, near midnight. The experiment became an impromptu investigation of postmidnight spread *F* which is common during solar minimum.

The Too WINDY observations differ from observations of postsunset spread *F* phenomena, as exemplified by the WINDY experiment which took place in 2017, in a number of ways. The *F* layer was low and rarefied throughout the observing window. The zonal plasma flow, as measured by the sounding rocket and inferred from the apparent motion of regions of coherent scatter, was irregular, especially in the topside. Most importantly, large-scale density irregularities were seen almost exclusively in the topside where they exhibited a zonal wavelength of approximately 200 km. The ALTAIR radar detected essentially no structuring in the bottomside, and the sounding rocket observed only very small bottomside density irregularities. Coherent scatter was observed mainly on the walls of topside irregularities.

The aforementioned characteristics are consistent with observations of postsunset ionospheric *F* region instability made by coherent scatter radars. Radar imagery from Jicamarca indicates that topside irregularities occur without obvious bottomside precursors and exhibit somewhat erratic zonal drifts that vary sharply in altitude and time. Morphologically, the irregularities resemble patches of small convective plumes. These could be excited by zonal winds traversing horizontal density gradients associated with large-scale topside structure, as is the case during ordinary postsunset spread *F*.

How convective instability can lead to topside structuring without deforming the bottomside is enigmatic. The structuring was not merely "fossil" structuring in nature as it clearly became more intense after the rocket launches. Two possible scenarios were investigated through numerical simulation. In one case, the background zonal electric field was increased above its climatological average. In another, intense forcing due to neutral waves and turbulence propagating from below was introduced in the simulation. Both cases led to *F*-region structuring. Neither case closely resembled the Too WINDY observations as the simulation always predicted more structuring in the bottomside than the topside. The latter simulation did however account for vertical shears in the topside zonal plasma drifts and also produced modest structuring in the topside density.

The event observed during Too WINDY appears to have been qualitatively distinct from postsunset spread *F* phenomenology that has been so long under investigation. Whether it is representative of **premidnight** spread *F* generally is unknown, but the record of coherent scatter observations suggests that it might be. The **premidnight spread *F*** problem is well suited for sounding rocket investigations since profiling is essential for identifying all the forcing and the plasma instabilities at work. A purpose-made sounding rocket investigation is warranted.

Acknowledgments. DLH appreciates the assistance of D. C. Fritts who provided the nuetral wind simulations that contributed to this work. This work was supported by award NNX15AL02G from the National Aeronautics and Space Administration and award FA9550-12-1-0462 from the Air Force Office of Scientific Research to Cornell University. The Jicamarca Radio Observatory is a facility of the Instituto Geofisíco del Perú operated with support from NSF award AGS-1732209 through Cornell. The help of the staff is much appreciated. Radar data used for this publication are available through the Madrigal database (see `http://www.openmadrigal.org`). Rocket data are available through the Goddard Space Flight Center Space Physics Data Facility (see `http://spdf.gsfc.nasa.gov`).

References

Aveiro, H. C., D. L. Hysell, R. G. Caton, K. M. Groves, J. Klenzing, R. F. Pfaff, R. Stoneback, and R. A. Heelis, Three-dimensional numerical simulations of equatorial spread *F*: Results and observations in the Pacific sector, *J. Geophys. Res.*, p. doi:10.1029/2010JA015602, 2012.

Chapagain, N. P., B. G. Fejer, and J. L. Chau, Climatology of postsunset equatorial spread *F* over Jicamarca, *J. Geophys. Res.*, p. doi:10.1029/2008JA013911, 2009.

Chen, L., O. Santolik, M. Hajos, L. Zheng, Z. Zhima, and R. Heelis, Source of the low-altitude hiss in the ionosphere, *Geophys. Res. Lett.*, *44*, 2060–2069, https://doi.org/10.1002/2016GL072,181, 2017.

Chen, L., R. F. Pfaff, R. Heelis, S. Bordsen, and Z. Xia, Ion cyclotron resonant absorption lines in ELF hiss power spectral density in the low-latitude ionosphere, *Geophys. Res. Lett.*, p. https://doi.org/10.1029/2019GL086315, 2020.

Drob, D. P., et al., An update to the Horizontal Wind Model (HWM): The quiet time thermosphere, *Earth and Space Science*, *2*, doi:10.1002/2014EA000,089, 2015.

Fejer, B. G., The electrodynamics of the low-latitude ionosphere: Recent results and future challenges, *J. Atmos. Terr. Phys.*, *59*, 1465–1482, 1997.

Gentile, L. C., W. J. Burke, and R. G. Rich, A global climatology for equatorial plasma bubbles in the topside ionosphere, *Ann. Geophys.*, *24*, 163–172, 2006.

Haerendel, G., and J. V. Eccles, The role of the equatorial electrojet in the evening ionosphere, *J. Geophys. Res.*, *97*, 1181, 1992.

Haerendel, G., J. V. Eccles, and S. Cakir, Theory for modeling the equatorial evening ionosphere and the origin of the shear in the horizontal plasma flow, *J. Geophys. Res.*, *97*, 1209, 1992.

Heelis, R. A., R. Stoneback, G. D. Earle, R. A. Haaser, and M. A. Abdu, Medium-scale equatorial plasma irregularities observed by the Coupled Ion-neutral Dynamics investigation on the Communication Navigation Outage Forecast System in a prolonged solar minimum, *J. Geophys. Res.*, *115*, doi:10.1029/2010JA015,596, 2010.

Huba, J. D., and J. Krall, Impact of meridional winds on equatorial spread *F*: Revisited, *Geophys. Res. Lett.*, *40*, 1268–1272, doi:10.1002/grl.50,292, 2013.

Hysell, D. L., and J. L. Chau, Optimal aperture synthesis radar imaging, *Radio Sci.*, *41*, 10.1029/2005RS003,383, RS2003, 2006.

Hysell, D. L., and E. Kudeki, Collisional shear instability in the eqautorial *F* region ionosphere, *J. Geophys. Res.*, *109*, (A11,301), 2004.

Hysell, D. L., R. Jafari, D. C. Fritts, and B. Laughman, Gravity wave effects on postsunset equatorial *F* region stability, *J. Geophys. Res.*, *119*, 5847–5860, doi:10.1002/2014JA019,990, 2014.

Hysell, D. L., M. F. Larsen, D. C. Fritts, B. Laughman, and M. P. Sulzer, Major upwelling and overturning in the mid-latitude f region ionosphere, *Nature Comm.*, *9*, 10.1038/s41,467–018–05,809–x, 2018.

Hysell, D. L., S. Rao, K. M. Groves, and M. F. Larsen, Radar investigation of postsunset equatorial ionospheric stability over Kwajalein during project WINDY, *J. Geophys. Res.*, p. https://doi.org/10.1029/2020ja027997, 2020.

Kelley, M. C., J. J. Makela, O. de la Beaujardiere, and J. Retterer, Convective ionospheric storms: A review, *Rev. Geophys.*, *49*, doi:10.1029/2010RG000,340, 2011.

Kintner, P. M., W. Scales, J. Vago, A. Yau, B. Whalen, R. Arnoldy, and T. Moore, Harmonic H+ gyrofrequency structures in auroral hiss observed by high-altitude auroral sounding rockets, *J. Geophys. Res.*, *96*, 9627–9638, https://doi.org/10.1029/91JA00,563, 1991.

Kudeki, E., B. G. Fejer, D. T. Farley, and H. M. Ierkic, Interferometer studies of equatorial *F* region irregularities and drifts, *Geophys. Res. Lett.*, *8*, 377, 1981.

Kudeki, E., A. Akgiray, M. A. Milla, J. L. Chau, and D. L. Hysell, Equatorial spread-F initiation: post-sunset vortex, thermospheric winds, gravity waves, *J. Atmos. Sol. Terr. Phys.*, *69 (17-18)*, 2416–2427, 2007.

Li, G., B. Ning, L. Liu, W. Wan, L. Hu, B. Zhao, and A. K. Patra, Equincotial and June solstitial *F*-region irregularities over Sanya, *Ind. J. Rad. Space Phys.*, *42*, 168–183, 2012.

Makela, J. J., M. C. Kelley, and O. Beaujardiere, Convective ionospheric storms: A major space weather problem, *Space Weather*, *4*, doi:10.1029/2005SW000,144, 2006.

Miyoshi, Y., S. Matsuda, S. Kurita, K. Nomura, K. Keika, M. Shoji, N. Kitamura, and Y. Kasahara, EMIC waves covnerted from equatorial noise due to M/Q=2 ions in the plasmasphere: Observatoins from Van Allen Probes and Arase, *Geophys. Res. Lett.*, *46*, 5662–5669, https://doi.org/10.1029/2019GL083,024, 2019.

Otsuka, Y., Review of the generation mechanisms of post-midnight irregularities in the equatorial and low-latitude ionosphere, *Prog. Earth Plan. Sci.*, *5*, https://doi.org/10.1186/s40,645–018–0212–7, 2018.

Otsuka, Y., T. Ogawa, and Effendy, VHF radar observations of *F*-region field-aligned irregularities over Kototabang, Indonesia, *Earth, Planets, and Space*, *61*, 431–437, https://doi.org/10.1186/BF03353,159, 2009.

Patra, A. K., D. V. Phanikumar, and T. K. Pant, Gadanka radar observations of F region field-aligned irregularities during June solstice of solar minimum: First results and preliminary analysis, *J. Geophys. Res.*, *114*, https://doi.org/10.1029/2009JA014,437, 2009.

Pfaff, R. F., C. Leibrecht, J.-J. Berthelier, M. Malingre, M. Parrot, and J.-P. Lebreton, DEMETER satellite observations of plasma irregularities in the topside ionosphere at low, middle, and sub-auroral latitudes and their dependence on magnetic storms, in *Midlatitude Ionospheric Dynamics and Disturbances*, vol. 181, p. https://doi.org/10.1029/181GM27, American Geophysical Union, 2008.

Retterer, J. M., Physics based forecasts of equatorial radio scintillation for the Communication and Navigation Outage Forecasting System (C/NOFS), *Space Weather*, *3*, doi:10.1029/2005SW000,146, 2005.

Scherliess, L., and B. G. Fejer, Radar and satellite global equatorial *F* region vertical drift model, *J. Geophys. Res.*, *105*, 6829–6842, 1999.

Stoneback, R. A., R. A. Heelis, A. G. Burrell, W. R. Coley, B. G. Fejer, and E. Pacheco, Observations of quiet time vertical ion drift in the equatorial ionosphere during the solar minimum period of 2009, *J. Geophys. Res.*, *116*, doi:10.1029/2011JA016,712, 2011.

Tsunoda, R. T., R. C. Livingston, and C. L. Rino, Evidence of a velocity shear in bulk plasma motion associated with the post-sunset rise of the equatorial *F* layer, *Geophys. Res. Lett.*, *8*, 807, 1981.

Woodman, R. F., Spread F- An old equatorial aeronomy problem finally resolved?, *Ann. Geophys.*, *27*, 1915–1934, 2009.

Woodman, R. F., and C. La Hoz, Radar observations of *F* region equatorial irregularities, *J. Geophys. Res.*, *81*, 5447–5466, 1976.

Zhan, W., F. S. Rodrigues, and M. A. Milla, On the genesis of postmidnight equatorial spread *F*: Results from the American/Peruvian sector, *Geophys. Res. Lett.*, *45*, 7354–7361, https://doi.org/10.1029/2018GL078,822, 2018.

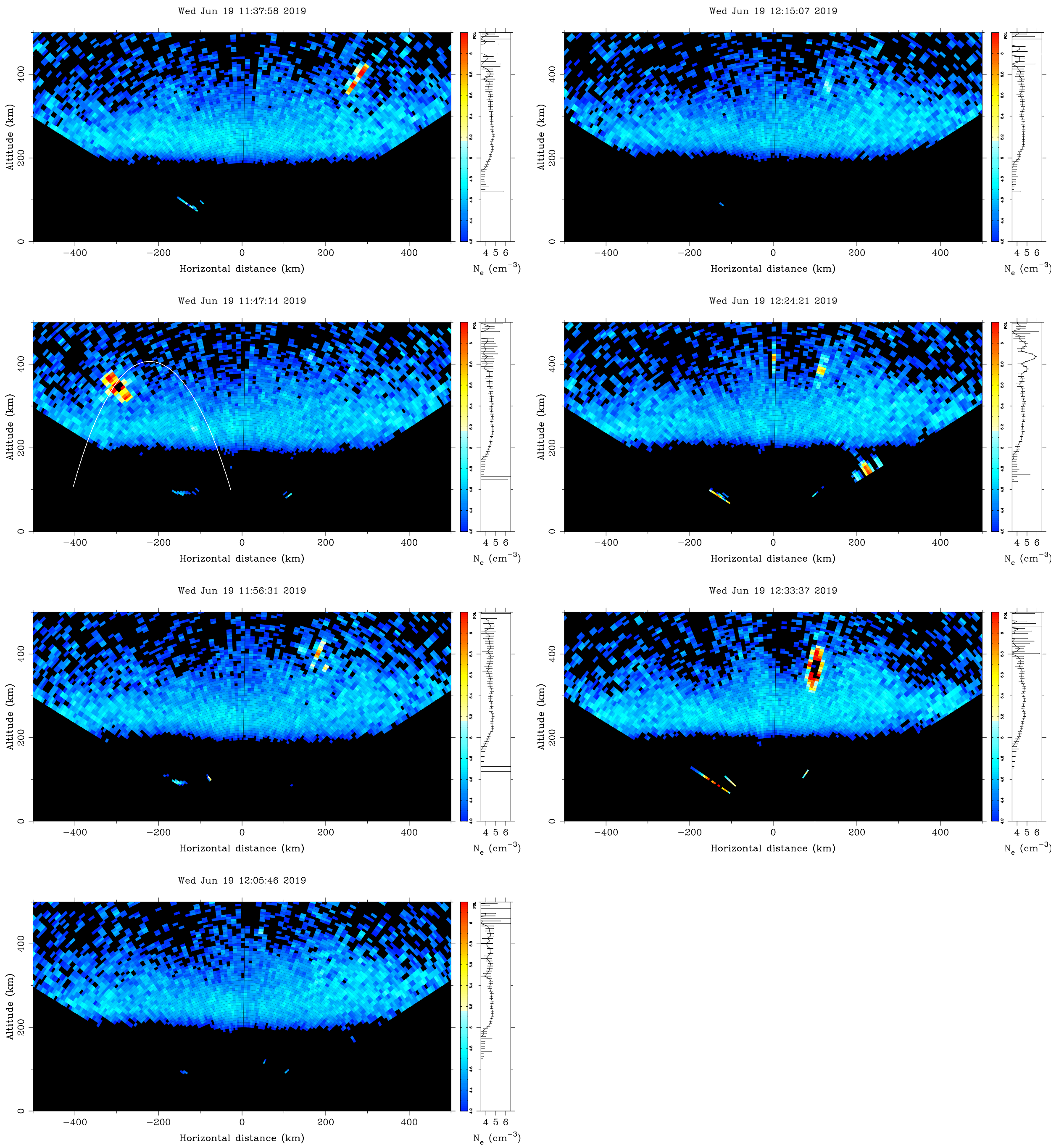

Figure 1. Sequence of UHF radar scans taken on June 19, 2019. The first scan began at 1126 UT, and the last scan ended at 1232 UT. Time advances from top to bottom, left to right.

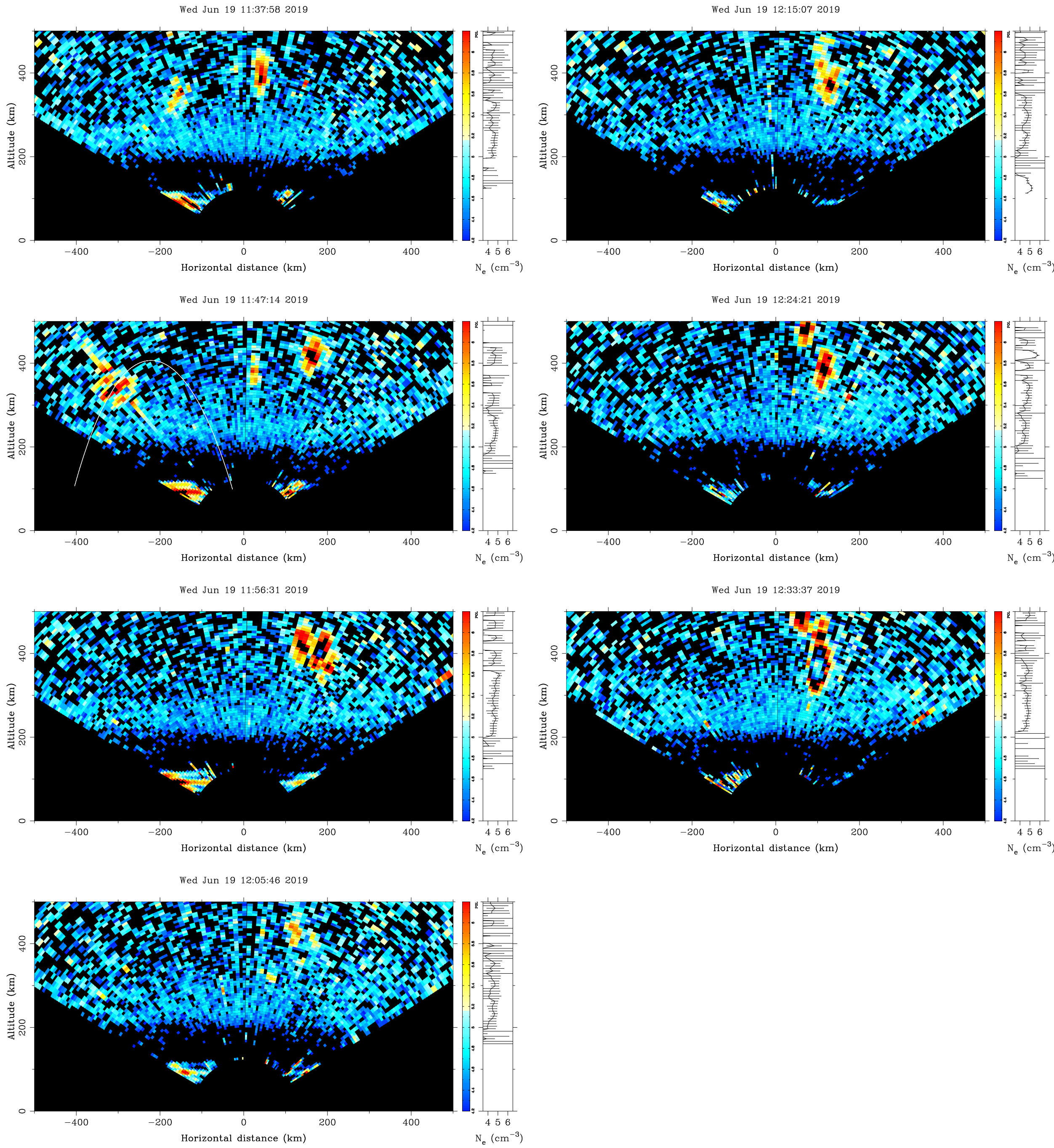

Figure 2. Same as Fig. 1 except for VHF scans.

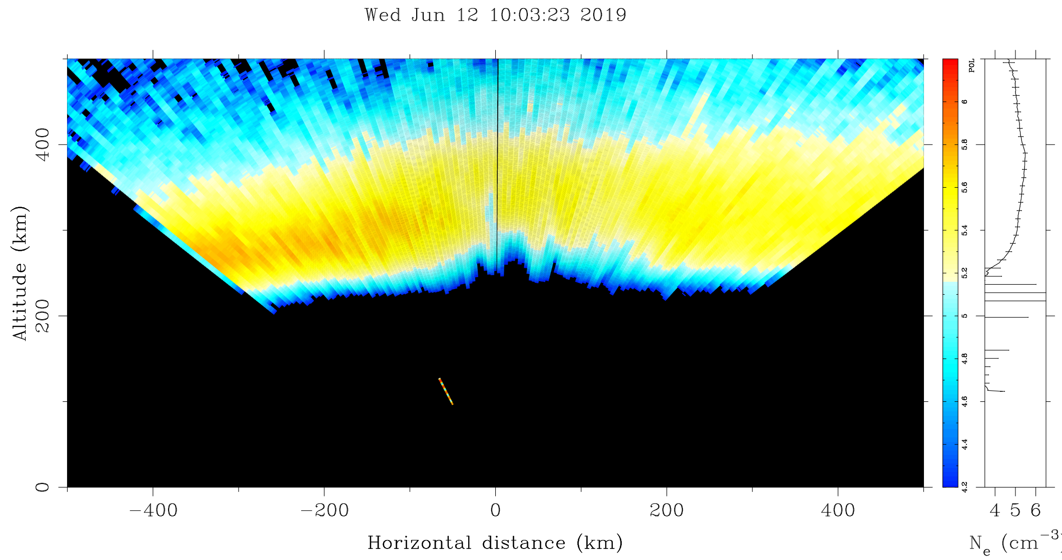

Figure 3. Oblique UHF scan of an ESF depletion observed on June 12, 2019.

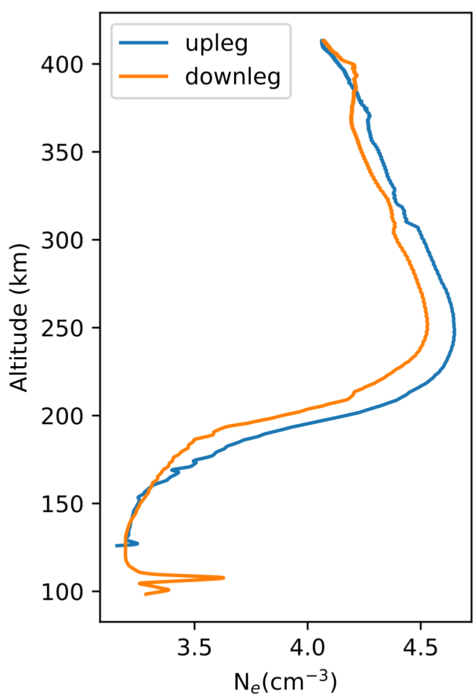

Figure 4. Electron density profiles measured by the Langmuir probe on the upleg and downleg of the instrumented rocket flight.

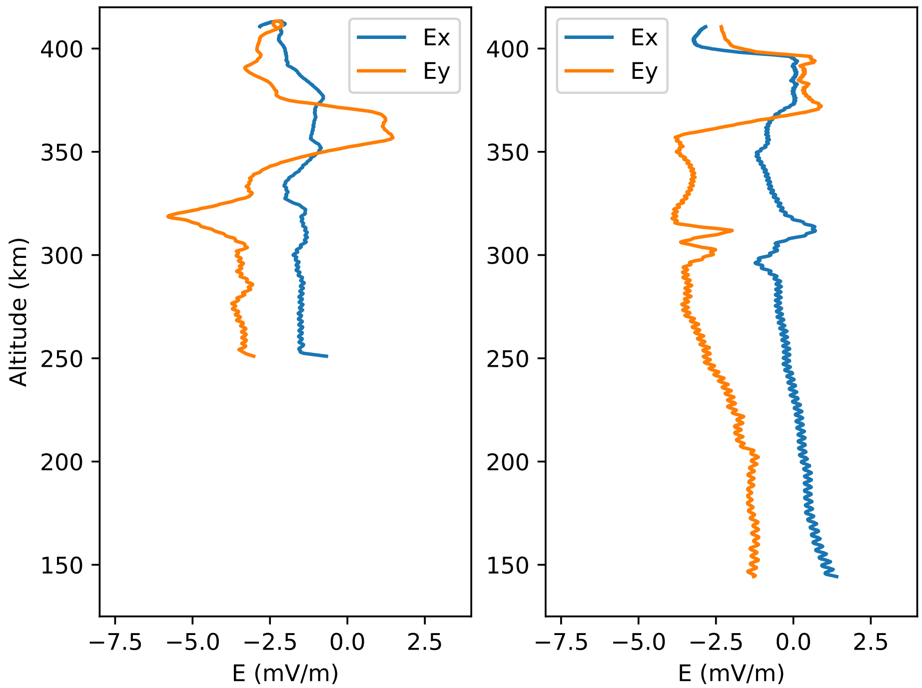

Figure 5. Vector electric fields measured by the e-field probes on the upleg (left) and downleg (right) of the instrumented rocket flight. Here, E_x and E_y refer to the zonal and vertical components of the electric field in the plane perpendicular to **B**. Note that the background magnetic field intensity at 350-km altitude is about 0.287×10^{-4} T above Kwajalein.

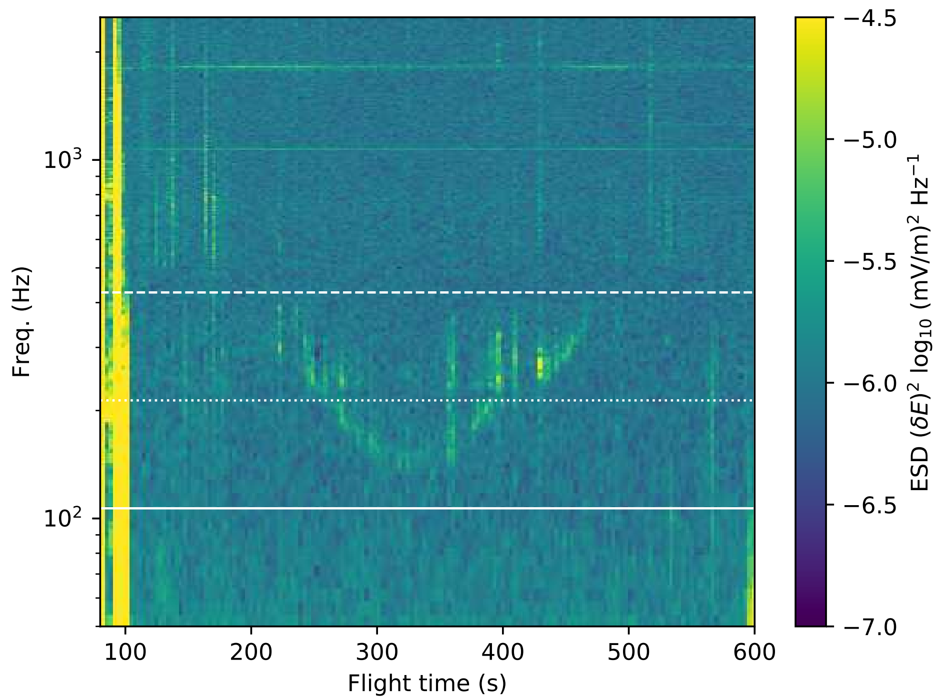

Figure 6. Spectrum of electric field fluctuations in the ELF band measured as a function of flight time. The solid, dashed, and long dashed lines indicate the gyroharmonic frequencies Ω_{He^+}, $2\Omega_{He^+}$, and Ω_{H^+}, respectively.

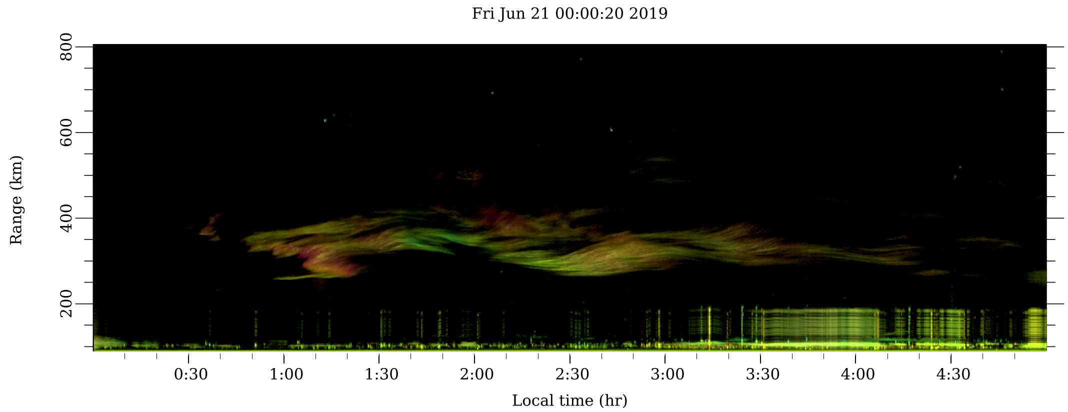

Figure 7. Range-time-intensity (RTI) plot of coherent scatter observed by the Jicamarca Radio Observatory in the postmidnight sector on June 21, 2019. Red and blue hues denote red and blue Doppler shifts between ± 150 m/s.

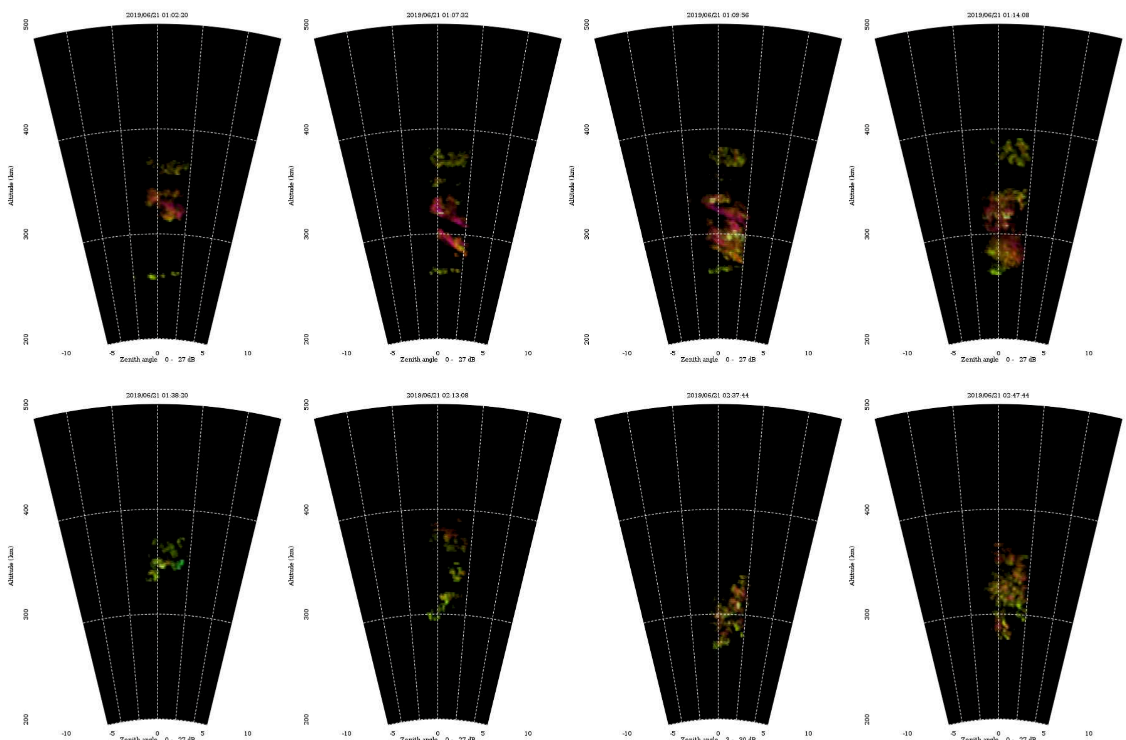

Figure 8. Aperture synthesis radar images of coherent scatter over Jicamarca on the morning of June 21, 2019. Animated sequences of images reveal a very complicated flow pattern characterized by strong vertical shear in the zonal flow and abrupt flow reversals in time.

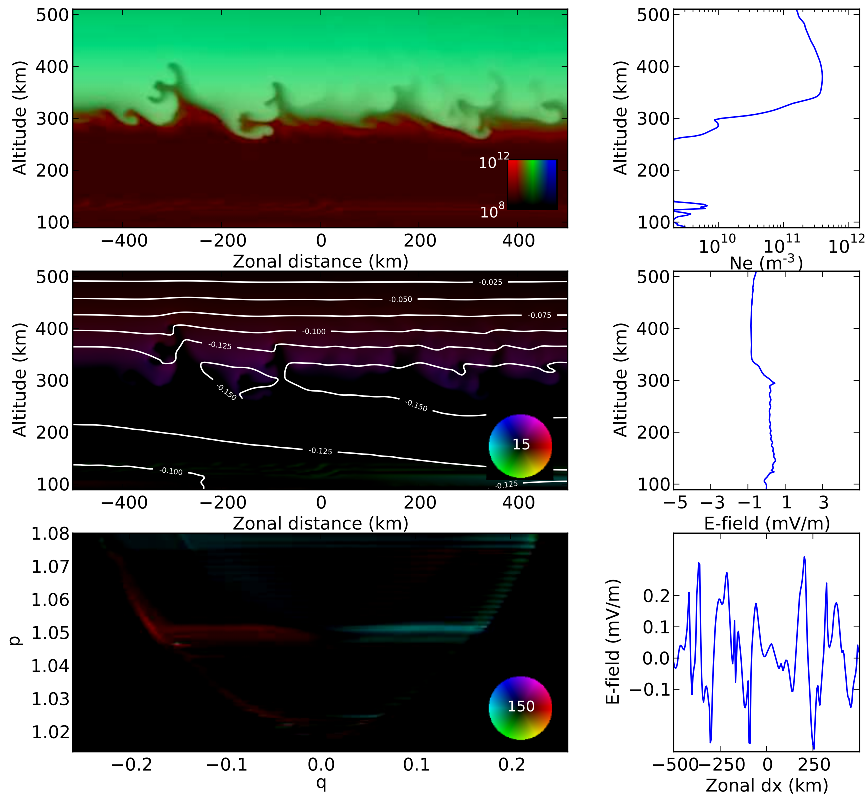

Figure 9. Numerical simulation of the ionosphere over Kwajalein under Too WINDY conditions. The top panel shows ion density in the equatorial plane, with red, green, and blue hues denoting molecular ions, atomic oxygen ions, and hydrogen ions, respectively. An electron density profile taken through the center of the panel appears to the right. The middle panel shows current density in the equatorial plane. The color wheel indicates the magnitude and direction with full scale being 15 nA/m^2. White contours are equipotentials. A vertical profile of the vertical electric field appears to the right. The bottom panel shows the current density in magnetic coordinates in the meridional plane bisecting the simulation. The color wheel indicates the magnitude and direction with full scale being 150 nA/m^2. A horizontal profile of the horizontal electric field at 300 km altitude appears to the right.

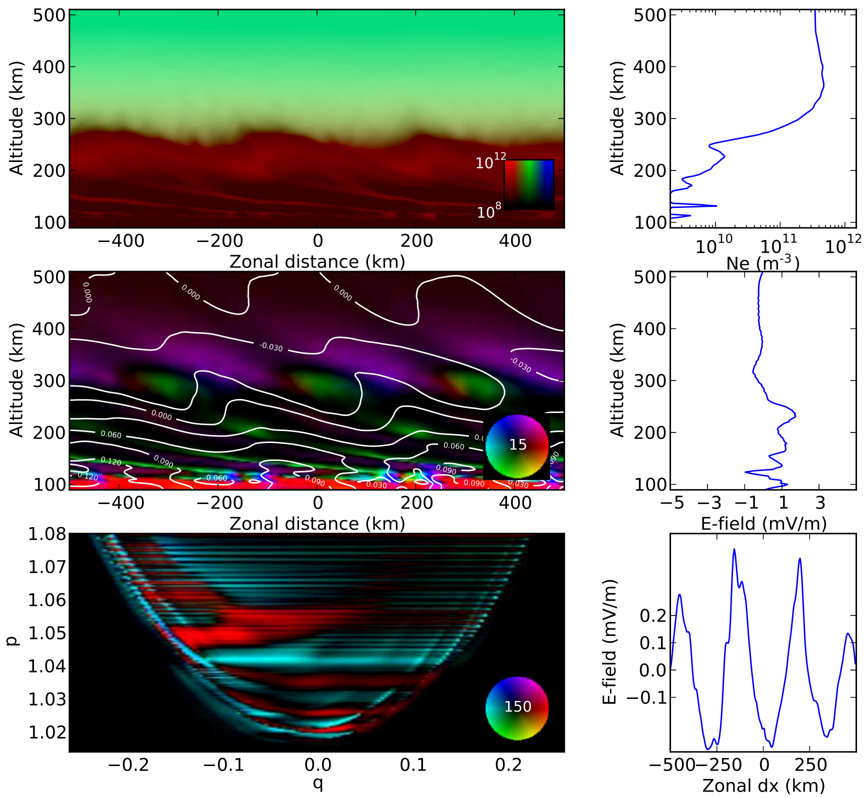

Figure 10. Similar to Fig. 9 only with forcing from neutral waves and turbulence.